Published in final edited form as:
J Magn Reson Imaging. 2015 February ; 41(2): 460–473. doi:10.1002/jmri.24551.

Fast Pediatric 3D Free-breathing Abdominal Dynamic Contrast Enhanced MRI with High Spatiotemporal Resolution

Tao Zhang, MS[1], **Joseph Y. Cheng, PhD**[1], **Aaron G. Potnick, MD**[2], **Richard A. Barth, MD**[2], **Marcus T. Alley, PhD**[2], **Martin Uecker, PhD**[3], **Michael Lustig, PhD**[3], **John M. Pauly, PhD**[1], and **Shreyas S. Vasanawala, MD, PhD**[2]

[1]Electrical Engineering, Stanford University, Stanford, California, USA.

[2]Radiology, Stanford University, Stanford, California, USA.

[3]Electrical Engineering and Computer Sciences, University of California, Berkeley, California, USA.

Abstract

Purpose—To develop a method for fast pediatric 3D free-breathing abdominal dynamic contrast enhanced (DCE) MRI and investigate its clinical feasibility.

Materials and Methods—A combined locally low rank parallel imaging method with soft gating is proposed for free-breathing DCE MRI acquisition. With IRB approval and informed consent/assent, 23 pediatric patients were recruited for this study. Free-breathing DCE MRI with approximately 1 mm^3 spatial resolution and 6.5 s frame rate was acquired on a 3T scanner. Undersampled data were reconstructed with a compressed sensing method without motion correction (FB-CS) and the proposed method (FB-LR). A follow-up respiratory-triggered acquisition (RT-CS) was performed as a reference standard. The reconstructed images were evaluated independently by two radiologists. Wilcoxon tests were performed to test the hypothesis that there was no significant difference between different reconstructions. Quantitative evaluation of contrast dynamics was also performed.

Results—The mean score of overall image quality of FB-LR was 4.0 on a 5-point scale, significantly better ($P<0.05$) than FB-CS reconstruction (mean score 2.9), and similar to RT-CS (mean score 4.1). FB-LR also matched the temporal fidelity of contrast dynamics with a root mean square error less than 5%.

Conclusion—Fast 3D free-breathing DCE MRI with high scan efficiency and image quality similar to respiratory-triggered acquisition is feasible in a pediatric clinical setting.

Keywords

Pediatric dynamic contrast enhanced abdominal MRI; Parallel imaging; Low rank; Compressed sensing

Correspondence to: Tao Zhang, Packard 208, 350 Serra Mall, Stanford, CA 94305, Phone: (650) 725-5638, Fax: (650) 723-8374, tao@mrsrl.stanford.edu.

INTRODUCTION

Multiphasic post-contrast MRI, or Dynamic Contrast Enhanced (DCE) MRI, is a standard component of abdominal MRI exams, most commonly used to detect and characterize mass lesions, but also assess renal function (1–5). 3D DCE MRI is often limited by two issues: compromised spatiotemporal resolution and motion artifacts. The former limitation is due to the fast contrast dynamics, usually lasting for only a few minutes, and the relative long data acquisition for each temporal phase. The smaller anatomical structures and faster hemodynamics make it even more challenging for pediatric DCE MRI. The second issue of motion is particularly difficult in pediatric patients, as voluntary suspension of breathing can be difficult to obtain. Thus, deep anesthesia with periods of suspended respiration is necessary to avoid motion artifacts (6). This process often requires intubating pediatric patients, which can increase anesthetic risk, preparation time, and recovery duration. An alternative approach is respiratory-triggered data acquisition. However the spatiotemporal resolution is then compromised since the data acquisition can only be triggered when the respiration falls within an accepted window. Further, obtaining adequate signal from a respiratory bellows can be time-consuming in smaller children, requiring careful adjustment of the position of the bellows.

To accelerate DCE MRI and achieve high spatiotemporal resolution, parallel imaging (PI) and compressed sensing (CS) can be used. PI uses multiple receiving coils to acquire data simultaneously. The different coil sensitivities of the coil arrays can be used to reconstruct undersampled datasets (7–9). However, PI is limited by its inherent SNR penalty for high accelerations. On the other hand, CS exploits the data redundancy (image sparsity) of MR images (10). CS can reconstruct pseudo-randomly undersampled data by solving a nonlinear optimization problem. Further acceleration of MR data acquisition can be achieved by combining PI and CS. DCE MRI using a combined parallel imaging compressed sensing method has been reported that can resolve arterial and venous phase in pediatric clinical setting with suspended respiration (11). However, the reported temporal resolution is approximately 20 s, still relatively poor compared to the contrast dynamics in pediatric patients. Deep anesthesia and suspended respiration are also required to ensure a good image quality.

To further accelerate DCE MRI, the spatiotemporal data correlation can be exploited. The data redundancy of DCE MRI is reflected by a strong spatiotemporal correlation in the DCE image series. This property of dynamic MRI is also known as the low rank property, studied by Liang, Haldar and others (12–15). Furthermore, since the hemodynamics of adjacent image pixels are often similar, there is more data redundancy within a local image region compared to the entire image (16–19). The low rank constraint can be used to reconstruct undersampled dynamic MRI datasets. The method that exploits the spatiotemporal correlation of the entire image is referred to as the globally low rank (GLR) method. The method that exploits the spatiotemporal correlation within a small image region is referred to as the locally low rank (LLR) method. Breath-held 3D DCE MRI with a very high acceleration (R = 19) can be achieved using the combination of LLR and PI (17).

Respiratory-triggering/gating can address the problem of respiratory motion, but the scan time will be significantly increased (usually by at least three-fold). With a careful ordering of the phase encoding, free-breathing acquisition with high scan efficiency can be achieved with relatively suppressed motion artifacts (20–22). Furthermore, with the knowledge of the respiratory motion, non-rigid motion correction methods can be applied to reduce residual motion artifacts (23–29). Recently, a soft gating method has been proposed (30). This method generates a motion-weighting function based on a navigator signal, and introduces a reconstruction with a motion-weighted data consistency (30, 31). The soft gating approach can reduce motion artifacts without intensive computation.

In this work, a combined locally low rank parallel imaging method with soft gating is proposed for fast 3D free-breathing DCE MRI with high spatiotemporal resolution. The proposed method is deployed clinically and compared with respiratory-triggered acquisitions.

MATERIALS AND METHODS

Autocalibrating Parallel Imaging with ESPIRiT

In PI, multiple receiving coils with different coil sensitivities are used to acquire data simultaneously. Define $\boldsymbol{y_t}$ as the acquired k-space data from all coils at temporal phase t, $\boldsymbol{m_t}$ as the reconstructed image at temporal phase t, $\boldsymbol{S}$ as the coil sensitivities, $\boldsymbol{\mathscr{F}}$ as the Fourier transform operator, $\boldsymbol{D_t}$ as the subsampling operator that selects the acquired data points at temporal phase t, and T as the total number of temporal phases in the DCE acquisition. Then, undersampled PI datasets can be reconstructed by minimizing the difference between the acquired data and the reconstructed image through the acquisition model:

$$\text{minimize}_{\boldsymbol{m_t}} \sum_{t=1}^{T} \| \boldsymbol{D_t \mathscr{F} S m_t} - \boldsymbol{y_t} \|_2^2. \quad [1]$$

To measure the coil sensitivities explicitly, an extra scan is required (7). However, accurate coil sensitivities are difficult to achieve, especially in abdominal MRI. Alternatively, autocalibrating parallel imaging acquires additional k-space points (8, 9) and uses the coil sensitivities implicitly. ESPIRiT (32) uses a similar autocalibrating approach and estimates the explicit coil sensitivities by an eigenvalue analysis. In this work, the coil sensitivities were calculated using ESPIRiT. To solve the problem with a reduced field of view in PI (33), two or more sets of eigenvector maps can be applied in ESPIRiT. Define $\boldsymbol{S_i}$ as multiple sets of ESPIRiT eigenvector maps (N_s eigenvector maps in total), and $\boldsymbol{m_t^i}$ as the i^{th} image components at temporal phase t. Then Eq. [1] can be reformulated as:

$$\text{minimize}_{\boldsymbol{m_t}} \sum_{t=1}^{T} \left\| \boldsymbol{D_t \mathscr{F}} \sum_{i}^{N_s} \boldsymbol{S_i m_t^i} - \boldsymbol{y_t} \right\|_2^2. \quad [2]$$

Locally Low Rank ESPIRiT for DCE MRI

To exploit the data redundancy of DCE image series, the DCE datasets can be reformatted into a spatiotemporal matrix, also known as the Casaroti matrix (16–19). Each column of the spatiotemporal matrix represents an image at one temporal phase. The spatiotemporal

correlation of the DCE acquisition is reflected by the low rank property of the spatiotemporal matrix. Furthermore, this matrix is even more rank-deficient if only a image region with similar dynamics is considered. This is known as the LLR method. An example of the LLR property of DCE MRI is shown in Fig. 1: 20 DCE images can be represented by only four principal components in each 16×16 image region. This LLR constraint can be combined with PI to reconstruct highly accelerated DCE datasets. Assume each image can be divided into N_b image blocks. Define $\boldsymbol{m}$ as the reconstructed image from all T temporal phases, $\boldsymbol{C_b}$ as an operator that selects an image block b and reformats it into a spatiotemporal matrix. Ignoring respiratory motion, the combined LLR and ESPIRiT method can be formulated as:

$$\begin{array}{l}\text{minimize}_{\boldsymbol{m}} \sum_{b=1}^{N_b} \|\boldsymbol{C_b m}\|_* \\ \text{subject to} \sum_{t=1}^{T} \|\boldsymbol{D_t} \mathscr{F} \sum_{i}^{N_s} \boldsymbol{S_i m_t^i} - \boldsymbol{y_t}\|_2^2 < \varepsilon,\end{array} \quad [3]$$

Where $\|A\|_*$ is the nuclear norm of a matrix A (sum of the singular values of A) (34), and ε is a parameter that controls data consistency (9). In general, small image blocks (size ranging from 8×8 to 16×16) are preferred for a lower rank of the spatiotemporal matrices (16). Singular value thresholding (SVT) algorithm can be used to minimize the nuclear norm of different image blocks (35). In our study, the threshold in SVT was empirically set to 0.005 of the largest singular values of each image block.

Soft-gated Locally Low Rank ESPIRiT

For a free-breathing abdominal acquisition, acquired data points are not consistent with a fixed respiratory motion state. A modified self-navigated 3D SPGR sequence (Butterfly) can be used to measure the respiratory motion from the data acquisition itself (25). With a careful ordering of the phase encodings by VDRad (21), the data acquisition will be potentially more robust to respiratory motion. A soft gating approach can further improve the image quality (30). First, a high pass filter is typically applied to the Butterfly navigator signal to remove the low-frequency drift due to contrast injection. The end of expiration is considered as motion free. Based on the estimated respiratory motion, the amount of motion inconsistency can be calculated, and a motion-weighting w ranging from 0 to 1 can be generated based on the following equation (30):

$$w = \begin{cases} e^{-\alpha(d - Thresh)}, d > Thresh \\ 1, \text{otherwise} \end{cases} \quad [4]$$

Where d represents the estimated S/I respiratory motion with respect to the end of expiration, *Thresh* is a threshold of the respiratory motion, and α is a scaling factor. Data points with S/I motion less than the threshold have a weighting of 1 and are considered to be motion free. Data points with bigger respiratory motion have less motion weighting. The parameters were experimentally tuned and then set the same for the rest of the study: 10% of the maximum S/I motion ($d_{\max}$) was set as the threshold and α was set to $3/d_{\max}$. Define $\boldsymbol{W_t}$ as the motion-weighting matrix at temporal phase t, the soft-gated Locally Low Rank ESPIRiT can be formulated as:

$$\begin{aligned} &\text{minimize}_{\boldsymbol{m}} \sum_{b=1}^{N_b} \|\boldsymbol{C_b m}\|_* \\ &\text{subject to} \sum_{t=1}^{T} \|\boldsymbol{W_t}(\boldsymbol{D_t}\mathscr{F}\sum_{i}^{N_s}\boldsymbol{S_i m_t^i} - \boldsymbol{y_t})\|_2^2 < \varepsilon. \end{aligned} \quad [5]$$

To demonstrate the concept of soft gating, an example of the soft-gated DCE acquisition with the VDRad ordering is shown in Fig. 2.

Patient Recruitment

With institutional review board approval and informed patient consent/assent, 23 consecutive patients (13 males and 10 females) referred for contrast enhanced abdominal MRI under sedation at our institution were recruited from June 2012 to July 2013. Patient demographics, types of respiratory support and clinical indications are summarized in Tab. 1. The patient age ranges from 6 weeks to 8.75 years (mean, 4.4 years).

Image Acquisition

All imaging was performed on a 3T MR750 scanner (GE Healthcare, Waukesha, WI, USA) with a commercially available 32-channel cardiac coil or torso coil. A multi-phase 3D modified SPGR sequence with motion navigation (Butterfly), intermittent spectrally selective fat-inversion pulses and VDRad sampling patterns were used during the contrast injection (36). Prescribed acquisition parameters were minimum echo time (TE) 1.2–1.6 ms, repetition time (TR) 3.0–3.7 ms, flip angle 15°, bandwidth (BW) 100 kHz, slice thickness 0.9–1.2 mm, S/I FOV 20–44 cm, spatial resolution 0.8×0.8–1.4×1.4 mm^2, and a total acceleration factor 7.8–8.0. The total acceleration factor is defined as the acceleration factor of a 3D dataset at a single temporal phase. The average acquisition time for each temporal phase was 6.5 s (range, 5.4–7.6 s). The details of acquisition parameters are shown in Tab. 1. Single dose Gadavist, Multihance, Ablavar or Eovist was diluted as necessary in saline to ensure a volume of at least 10 mL and power injected intravenously at 1mL/s rate when possible and hand injected at approximately 1 mL/s when not. Contrast injection was initiated after the first temporal phase. Immediately following the multi-phase acquisition, a respiratory-triggered acquisition with similar acquisition parameters was performed. The average frame rate for the respiratory-triggered acquisition was approximately 44.0 s (range, 36.9–52.4 s).

Image Reconstruction

For each undersampled free-breathing multi-phase dataset, three reconstructions were performed: (a) a zero-filling reconstruction, (b) a combined compressed sensing parallel imaging (37) without motion correction performed for each phase individually with a view sharing of two adjacent temporal phases and (c) the proposed soft-gated Locally Low Rank ESPIRiT reconstruction. The zero-filling reconstruction has the temporal fidelity of the contrast enhancements and was used as the reference for the evaluation of contrast dynamics. The combined compressed sensing parallel imaging method is routinely used at our institution as the reconstruction method for accelerated imaging. The proposed method was solved with a projection onto convex sets (POCS) type algorithm and implemented in C/C++. The reconstruction time for each DCE dataset with the proposed method was approximately 10–15 minutes on a 24-core PC with 64 GB RAM. The ESPIRiT eigenvector

maps (coil sensitivities) were calculated from the time-averaged data. Two sets of eigenvector were used in the combined compressed sensing parallel imaging method and the proposed method. Image blocks with a size of 16×16 were used in the proposed method for all datasets. The details of the POCS-type algorithm can be found in references (9, 17, 18, 38–41). Coil compression (42) from 32 channels to 6 virtual channels was performed prior to all reconstructions to shorten the reconstruction time. For the post-contrast respiratory-triggered datasets, the combined compressed sensing parallel imaging was performed. For simplicity, for the rest of the paper, the free-breathing combined compressed sensing parallel imaging reconstruction is referred to as the free-breathing compressed sensing reconstruction (FB-CS), the free-breathing soft-gated Locally Low Rank ESPIRiT reconstruction is referred to as the free-breathing low rank reconstruction (FB-LR), and the respiratory-triggered combined compressed sensing parallel imaging was referred to as the respiratory-triggered compressed sensing reconstruction (RT-CS).

Image Evaluation

Two pediatric radiologists (S.S.V. and A.G.P. with 8 and 5 years of clinical experience with MR imaging respectively) who were blinded to patient history/diagnoses independently assessed the FB-CS, FB-LR and RT-CS reconstructions qualitatively. The images were assessed for overall image quality, degree of non-cardiac motion artifacts, and the quality of delineation of several anatomical structures (hepatic artery, right hepatic vein, diaphragm, and adrenal gland). The delineation of hepatic artery was evaluated only for the FB-CS and FB-LR reconstruction, as the respiratory-triggered images were obtained in the venous phase. The scoring criteria are shown in Tab. 2. Because of the readily apparent difference between different reconstructions, images were presented to the radiologists without blinding. First, the radiologists were asked to evaluate the reconstructions individually. Next, they were asked for the preference of side-by-side paired comparisons on overall image quality, degree of non-cardiac motion ghosts and structural delineation based on the criteria shown in Tab. 3.

Individual Qualitative Image Assessments—A paired Wilcoxon test was performed to assess the null hypothesis that there was no significant difference in overall image quality, degree of motion ghosts and structural delineation between FB-CS and FB-LR, FB-CS and RT-CS, and FB-LR and RT-CS, when images were assessed individually. A P value of 0.05 was used as a criterion of statistical significance.

Paired Qualitative Image Assessments—For evaluations with images shown side-by-side in pairs, a paired Wilcoxon test was performed to assess the null hypothesis that there was no significant preference between FB-CS and FB-LR, FB-CS and RT-CS, and FB-LR and RT-CS. A P value of 0.05 was used as a criterion of statistical significance.

Inter-observer Agreement—Inter-observer agreements between the two readers for all assessments were analyzed using the weighted kappa coefficients. The weighted kappa coefficients were interpreted as almost perfect (0.8–1), substantial (0.6–0.8), moderate (0.4–0.6), fair (0.2–0.4), slight (0–0.2) and poor (<0).

Quantitative Analysis of Contrast Dynamics—To evaluate the contrast dynamics of FB-CS and FB-LR, the zero-filling reconstruction was used as the reference. Manual segmentations of abdominal aorta and liver were performed on three reconstructions for each case. The normalized signal intensity of the segmented region was calculated for each reconstruction. To quantify the similarity of the contrast dynamics (signal intensity curve) of different reconstructions, the root mean square error (RMSE) of the contrast dynamics with respect to the reference was calculated for FB-CS and FB-LR according to the following equation:

$$\mathrm{RMSE}=\sqrt{\frac{\sum_{t=1}^{T}(\hat{x}_t - x_t)^2}{T}}, \quad [5]$$

where $\hat{x}_t$ is the signal intensity of FB-CS or FB-LR at time *t*, and x_t is the signal intensity of the zero-filling reconstruction at time *t*. To evaluate the contrast dynamics of smaller structures, the cross correlation of the contrast enhancement of the renal artery and abdominal aorta in the FB-LR reconstruction was also calculated. The renal artery in the zero-filling reconstruction and FB-CS was often not well delineated, and therefore was not segmented. The number of temporal phases in FB-CS and FB-LR where the hepatic artery was brighter than the hepatic vein was also recorded by one of the radiologists. Because of the variable-density sampling pattern applied in the data acquisition, the center k-space data that contained most of the contrast dynamics information were repeatedly acquired for each temporal phase. Both FB-CS and FB-LR enforced data consistency or motion-weighted data consistency with the data acquisition that should preserve the contrast dynamics.

RESULTS

Image Reconstruction

Figure 3 shows representative reconstructions of FB-CS, FB-LR and RT-CS for overall image quality and degree of motion ghosts. Figure 4 shows representative results of the delineation of several structures: (a) hepatic artery, (b) hepatic vein and diaphragm, and (c) adrenal gland. Because of the VDRad ordering, FB-CS reconstruction was already relatively robust against motion artifacts. As seen from Fig. 3, FB-CS, FB-LR and RT-CS had a similar degree of coherent non-cardiac motion ghosts. With soft gating and locally low rank constraints, FB-LR significantly reduced the residual motion artifacts. The image quality was similar to a respiratory-triggered acquisition. The DCE image series with FB-LR of a 6-year-old patient are shown in Fig. 5. The high spatial resolution is reflected by the sharp delineation of various anatomical structures, and the fine temporal resolution is reflected by the rapid progressive enhancement of the left kidney and spleen. Together, this demonstrates the feasibility of fast free-breathing 3D DCE pediatric MRI with high scan efficiency.

Image Evaluation

Individual Qualitative Image Assessments—The results of the Wilcoxon tests of all individual assessments are demonstrated in Fig. 6.

Overall Image Quality: All cases with the FB-LR and RT-CS reconstruction had diagnostically acceptable image quality for both readers. The mean scores for FB-CS, FB-LR and RT-CS were 3.0, 4.0 and 4.2 respectively for reader 1, and 2.8, 4.0 and 4.1 for reader 2. Based on the Wilcoxon test results, FB-LR and RT-CS had significantly better overall image quality than FB-CS for both readers. The difference between FB-LR and RT-CS did not reach a statistically significant level for any reader.

Degree of Non-cardiac Motion Ghosts: All cases with the FB-LR and RT-CS reconstruction did not have severe non-cardiac motion ghosts for both readers. The mean scores for FB-CS, FB-LR and RT-CS were 3.8, 4.1 and 4.1 respectively for reader 1, and 3.2, 4.0 and 4.1 for reader 2. Based on the Wilcoxon test results, FB-LR and RT-CS had significantly less motion ghosts than FB-CS for both readers. The difference between FB-LR and RT-CS again did not reach a statistically significant level for any reader. Note that cardiac motion ghosts were not assessed in this study.

Hepatic Artery: 22 out of 23 cases with the FB-LR reconstruction had diagnostically acceptable delineation of hepatic artery for both readers, compared to 12 cases with the FB-CS reconstruction. The mean scores for FB-CS and FB-LR were 2.5 and 3.9 respectively for reader 1, and 2.8 and 4.1 for reader 2. The delineation of hepatic artery with FB-LR was significantly better than FB-CS for both readers.

Hepatic Vein: 15 and 20 out of 23 cases with the FB-LR reconstruction had diagnostically acceptable delineation of hepatic vein for reader 1 and reader 2 respectively, compared to 3 and 5 cases with FB-CS and 18 and 19 cases with RT-CS. The mean scores for FB-CS, FB-LR and RT-CS were 1.5, 3.5 and 3.9 respectively for reader 1, and 2.1, 3.6 and 3.9 for reader 2. FB-LR and RT-CS had significantly better delineation than FB-CS for both readers. The difference between FB-LR and RT-CS did not reach a statistically significant level for any reader.

Diaphragm: 7 and 11 out of 23 cases with the FB-LR reconstruction had diagnostically acceptable delineation of diaphragm for reader 1 and reader 2 respectively, compared to 1 and 0 cases with FB-CS and 10 and 15 cases with RT-CS. The mean scores for FB-CS, FB-LR and RT-CS were 1.4, 2.5 and 2.3 respectively for reader 1, and 1.3, 2.1 and 3.0 for reader 2. FB-LR and RT-CS had significantly better delineation than FB-CS for both readers. For reader 2, RT-CS had significantly better delineation than FB-LR. The difference between FB-LR and RT-CS did not reach a statistically significant level for reader 1.

Adrenal Gland: 22 and 23 out of 23 cases with the FB-LR reconstruction had diagnostically acceptable delineation of adrenal gland for reader 1 and reader 2 respectively, compared to 22 and 18 cases with FB-CS and 22 and 22 cases with RT-CS. The mean scores for FB-CS, FB-LR and RT-CS were 3.6, 4.3 and 4.4 respectively for reader 1, and 3.4, 4.3 and 4.2 for reader 2. FB-LR and RT-CS had significantly better delineation than FB-CS for both readers. The difference between FB-LR and RT-CS did not reach a statistically significant level for any reader.

Paired Qualitative Image Assessments—The results of the Wilcoxon tests of all paired assessments are demonstrated in Fig. 7.

Overall Image Quality: Based on the Wilcoxon test results, the overall image quality of FB-LR and RT-CS was significantly superior compared to FB-CS for both readers. There was no significant preference between FB-LR and RT-CS for any reader.

Degree of Non-cardiac Motion Ghosts: The non-cardiac motion ghosts of FB-LR and RT-CS was significantly less compared to FB-CS for both readers. There was no significant preference between FB-LR and RT-CS for any reader.

Structural Delineation: The results of all four structures (hepatic artery, hepatic vein, diaphragm and adrenal gland) were combined together for the preference of structural delineation in Fig. 7. Compared to FB-CS, both readers preferred FB-LR and RT-CS for all structural delineation. Both readers preferred RT-CS to FB-LR for the delineation of diaphragm. Reader 1 preferred RT-CS to FB-LR for the delineation of hepatic vein. The preference between RT-CS and FB-LR on the other structures did not reach a significantly level for any reader.

Inter-observer Agreement—Results of inter-observer agreement on all individual and paired assessments based on the weighted kappa coefficients are shown in Tab. 4. Two readers had moderate to almost perfect agreement on all individual assessments. The inter-observer agreements for the preference of different reconstructions in all paired assessments varied from fair to almost perfect except the delineation of hepatic artery (poor inter-observer agreement).

Quantitative Analysis of Contrast Dynamics—The results of the quantitative analysis of contrast dynamics of FB-CS and FB-LR are shown in Tab. 5. An example of the contrast enhancement curves of the abdominal aorta and liver is shown in Fig. 5(b). A good agreement of contrast dynamics between the zero-filling reconstruction, FB-CS and FB-LR was observed in the evaluations, reflected by the small RMSEs: the mean RMSEs of the contrast dynamics in abdominal aorta were 0.045 (range: 0.031–0.082) and 0.050 (range: 0.017–0.068) for FB-CS and FB-LR respectively; the mean RMSEs of the contrast dynamics in liver were 0.019 (range: 0.009–0.034) and 0.020 (range: 0.007–0.032) for FB-CS and FB-LR respectively. The number of temporal phases in FB-CS and FB-LR where the hepatic artery was brighter than the hepatic vein also matched each other and evidenced the high temporal resolution. The high cross correlation of the contrast enhancements between renal artery and abdominal aorta in FB-LR (mean: 0.997; range: 0.993–0.999) showed the reasonable contrast enhancement of small structures in FB-LR that cannot be assessed in the zero-filling reconstruction or FB-CS.

DISCUSSION

This study addresses the salient challenges of fast free-breathing 3D DCE pediatric MRI. A soft-gated Locally Low Rank ESPIRiT method was proposed to reconstruct highly-undersampled free-breathing DCE datasets. The clinical performance of the proposed

method was investigated. The results of individual assessments suggest that FB-LR can provide overall image quality, degree of motion ghosts and structural delineation close to a respiratory-triggered acquisition (except the delineation of diaphragm). Based on our results, a similar overall image quality and degree of structural delineation are not likely to be achieved by a traditional compressed sensing reconstruction without motion correction. The paired assessment results also suggest that there is no clear preference between FB-LR and RT-CS. Together, the evaluation results demonstrate the feasibility of fast free-breathing DCE pediatric MRI. Compared to respiratory-triggered acquisition, the scan efficiency can be significantly improved by a free-breathing acquisition (more than 6-fold in this study). The proposed method also achieves a good spatiotemporal resolution that can depict small rapidly enhancing structures in a small child with rapid hemodynamics, which is not possible for respiratory-triggered acquisitions.

Because of the VDRad sampling pattern used in this study, respiratory motion artifacts have already been reduced without any motion correction. This is reflected by a close to clinically acceptable image quality in the FB-CS reconstruction, as well as a good delineation of the adrenal gland. The soft gating method has significantly reduced the remaining motion artifact, reflected by the improved scores in FB-LR. In this study, light sedation was still used to ensure a regular respiratory waveform and thus proper motion weighting. The respiratory support was reduced from our usual prior practice of endotracheal intubation to laryngeal mask or nasal cannula for most of the patients in this study. The proposed method is not very sensitive to the image block size. Similar results with block size ranging from 8×8 to 16×16 were observed. However, as discussed in Ref. (16) image blurring artifact may appear for very big image blocks, such as the entire image.

There were several limitations of this study. First, the study lacked the blinding of different images reconstructions. Blinding is difficult to achieve since the differences between the reconstructions with and without motion correction were obvious to the readers. It was also easy to differentiate free-breathing DCE acquisition and respiratory-triggered post-contrast acquisition because of the contrast dynamics and different number of temporal phases.

Second, the proposed method combines the advantages of the VDRad sampling method, the locally low rank method, parallel imaging, and soft gating. Each method contributes partly to the improved image quality of FB-LR than traditional DCE methods. Reconstructions with each individual method have not been evaluated separately in our study. These evaluations will be our future work.

Another limitation of this study was the quantitative evaluation of the contrast dynamics. Due to the rapid hemodynamics, it is impossible to acquire a fully sampled dataset to record the ground truth of the contrast dynamics. A zero-filling reconstruction of the undersampled datasets was used to provide a reference of the contrast dynamics of large structures, such as abdominal aorta and liver. However, due to the high acceleration applied in this study, the zero-filling reconstruction with low spatial resolution cannot provide with the reference of contrast dynamics for smaller structures. An alternative is to apply the modeling of contrast dynamics to the reconstructions (43) and investigate the calculated kinetic parameters. This

may provide a quantitative measurement of the contrast dynamics and will also be our future work.

In conclusion, this work shows the feasibility of fast free-breathing 3D DCE pediatric MRI with very high scan efficiency. The proposed FB-LR method can achieve similar image quality and structural delineation to respiratory-triggered acquisitions, but significantly improves the scan efficiency that results in a high spatiotemporal resolution. The proposed method can potentially address the two challenges of high spatiotemporal resolution and respiratory motion in pediatric abdominal DCE MRI.

Supplementary Material

Refer to Web version on PubMed Central for supplementary material.

ACKNOWLEDGEMENTS

The authors thank Dr. Alex McMillan for the help with the statistical analysis in this study.

Grant Sponsors: This work was supported by NIH grants R01 EB009690, P41 EB015891, UL1 TR000093, the Tashia and John Morgridge Faculty Scholars Fund, and GE Healthcare.

REFERENCES

1. Olsen OE. Imaging of abdominal tumours: CT or MRI? Pediatr Radiol. 2008; 38(Suppl 3):452–458. [PubMed: 18265967]
2. Darge K, Anupindi SA, Jaramillo D. MR imaging of the abdomen and pelvis in infants, children, and adolescents. Radiology. 2011; 261:12–29. [PubMed: 21931139]
3. Vasanawala SS, Lustig M. Advances in pediatric body MRI. Pediatr Radiol. 2011; 41(Suppl 2):549–554. [PubMed: 21847737]
4. Jones RA, Easley K, Little SB, Scherz H, Kirsch AJ, Grattan-Smith JD. Dynamic contrast-enhanced MR urography in the evaluation of pediatric hydronephrosis: Part 1, functional assessment. AJR AM J Roentgenol. 2005; 185:1598–1607. [PubMed: 16304021]
5. Griffin M, Grist TM, François CJ. Dynamic four-dimensional MR angiography of the chest and abdomen. Magn Reson Imaging Clin N Am. 2009; 17:77–90. [PubMed: 19364601]
6. Sury MR, Smith JH. Deep sedation and minimal anesthesia. Paediatr Anaesth. 2008; 18:18–24. [PubMed: 18095961]
7. Pruessmann KP, Weiger M, Scheidegger MB, Boesiger P. SENSE: sensitivity encoding for fast MRI. Magn Reson Med. 1999; 42:952–962. [PubMed: 10542355]
8. Griswold MA, Jakob PM, Heidemann RM, et al. Generalized autocalibrating partially parallel acquisitions (GRAPPA). Magn Reson Med. 2002; 47:1202–1210. [PubMed: 12111967]
9. Lustig M, Pauly JM. SPIRiT: iterative self-consistent parallel imaging reconstruction from arbitrary k-space. Magn Reson Med. 2010; 64:457–471. [PubMed: 20665790]
10. Lustig M, Donoho D, Pauly JM. Sparse MRI: The application of compressed sensing for rapid MR imaging. Magn Reson Med. 2007; 58:1182–1195. [PubMed: 17969013]
11. Zhang T, Chowdhury S, Lustig M, Barth RA, Alley MT, Grafendorfer T, Calderon PD, Robb FJL, Pauly JM, Vasanawala SS. Clinical performance of contrast enhanced abdominal pediatric MRI with fast combined parallel imaging compressed sensing reconstruction. J Magn Reson Imaging. 2013
12. Pedersen H, Kozerke S, Ringgaard S, Nehrke K, Kim WY. k-t PCA: temporally constrained k-t BLAST reconstruction using principal component analysis. Magn Reson Med. 2009; 62:706–716. [PubMed: 19585603]

13. Liang, ZP. Spatiotemporal imaging with partially separable functions; Proceedings of IEEE Int Symp Biomed Imag; Arlington. 2007. p. 988-991.
14. Lingala S, Hu Y, DiBella E, Jacob M. Accelerated dynamic MRI exploiting sparsity and low-rank structure: k-t SLR. IEEE Trans Med Imaging. 2011; 30:1042–1054. [PubMed: 21292593]
15. Haldar, JP.; Liang, ZP. Low-rank approximations for dynamic imaging; Proceedings of IEEE Int Symp Biomed Imag; Chicago. 2011. p. 1052-1055.
16. Trzasko, J.; Manduca, A. Local versus global low-rank promotion in dynamic MRI series reconstruction; Proceedings of the 19th Annual Meeting of ISMRM; Montreal. 2011. p. 4371
17. Zhang, T.; Alley, MT.; Lustig, M.; Li, X.; Pauly, JM.; Vasanawala, SS. Fast 3D DCE-MRI with sparsity and low-rank enhanced SPIRiT (SLR-SPIRiT); Proceedings of the 21st Annual Meeting of ISMRM; Salt Lake City. 2013. p. 2624
18. Zhang, T.; Pauly, JM.; Levesque, IR. Accelerating Parameter Mapping with a Locally Low Rank Constraint; Proceedings of the 21st Annual Meeting of ISMRM; Salt Lake City. 2013. p. 2458
19. Luo, J.; Shin, T.; Zhang, T.; Hu, B.; Nishimura, D. Lower extremities perfusion imaging with low-rank matrix completion reconstruction; Proceedings of the 21st Annual Meeting of ISMRM; Salt Lake City. 2013. p. 2619
20. Jhooti P, Wiesmann F, Taylor AM, et al. Hybrid ordered phase encoding (HOPE): an improved approach for respiratory artifact reduction. J Magn Reson Imaging. 1998; 8:968–980. [PubMed: 9702900]
21. Cheng, JY.; Zhang, T.; Alley, MT.; Lustig, M.; Vasanawala, SS.; Pauly, JM. Variable-density radial view-ordering and sampling for time-optimized 3D Cartesian imaging; Proceedings of the ISMRM Workshop on Data Sampling and Image Reconstruction; Sedona. 2013.
22. Doneva, M.; Stehning, C.; Nehrke, K.; Börnert, P. Improving scan efficiency of respiratory gated imaging using compressed sensing with 3D Cartesian golden angle sampling; Proceedings of the 19th Annual Meeting of ISMRM; Montréal. 2011. p. 3057
23. Schmidt JFM, Buehrer M, Boesiger P, Kozerke S. Nonrigid retrospective respiratory motion correction in whole-heart coronary MRA. Magn Reson Med. 2011; 15:551–564.
24. Ingle, RR.; Wu, HH.; Addy, NO.; Cheng, JY.; Hu, BS.; Nishimura, DG. Autofocusing nonrigid respiratory motion correction for 3D cones coronary MR angiography; Proceedings of the 21st Annual Meeting of ISMRM; Salt Lake City. 2013. p. 189
25. Cheng JY, Alley MT, Cunningham CH, Vasanawala SS, Pauly JM, Lustig M. Nonrigid motion correction in 3D using autofocusing with localized linear translation. Magn Reson Med. 2012; 68:1785–1797. [PubMed: 22307933]
26. Odille F, Vuissoz PA, Marie PY, Felblinger J. Generalized reconstruction by inversion of coupled systems (GRICS) applied to free-breathing MRI. Magn Reson Med. 2008; 60:146–157. [PubMed: 18581355]
27. Buerger C, Schaeffter T, King AP. Hierarchical adaptive local affine registration for fast and robust respiratory motion estimation. Medical Image Analysis. 2011; 15:551–564. [PubMed: 21454119]
28. Schmidt JFM, Buehrer M, Boesiger P, Kozerke S. Nonrigid retrospective respiratory motion correction in whole-heart coronary MRA. Magn Reson Med. 2011; 66:1541–1549. [PubMed: 21604297]
29. Batchelor PG, Atkinson D, Irarrazaval P, Hill DLG, Hajnal J, Larkman D. Matrix description of general motion correction applied to multishot images. Magn Reson Med. 2005; 54:1273–1280. [PubMed: 16155887]
30. Cheng, JY.; Uecker, M.; Alley, MT.; Vasanawala, SS.; Pauly, JM.; Lustig, M. Free-breathing pediatric imaging with nonrigid motion correction and parallel imaging; Proceedings of the 21st Annual Meeting of ISMRM; Salt Lake City. 2013. p. 312
31. Johnson KM, Block WF, Reeder SB, Samsonov A. Improved least squares MR image reconstruction using estimates of k-space data consistency. Magn Reson Med. 2012; 67:1600–1608. [PubMed: 22135155]
32. Uecker M, Lai P, Murphy MJ, et al. ESPIRiT – an eigenvalue approach to autocalibrating parallel MRI: where SENSE meets GRAPPA. Magn Reson Med. 2013

33. Griswold MA, Kannengiesser S, Heidemann RM, Wang J, Jakob PM. Field-of-view limitations in parallel imaging. Magn Reson Med. 2004; 52:1118–1126. [PubMed: 15508164]
34. Candès E, Recht B. Exact matrix completion via convex optimization. Found Comput Math. 2009; 9:717–772.
35. Cai J, Candès E, Shen Z. A singular value thresholding algorithm for matrix completion. SIAM J. OPTIM. 2010; 20:1956–1982.
36. Alley, MT.; Murphy, MJ.; Keutzer, K., et al. Improved time-resolved, 3D phase contrast imaging through variable Poisson sampling and partial respiratory triggering; Proceedings of the 19th Annual Meeting of ISMRM; Montreal. 2011. p. 1218
37. Uecker, M.; Virtue, P.; Vasanawala, SS.; Lustig, M. ESPIRiT reconstruction using soft SENSE; Proceedings of the 21st Annual Meeting of ISMRM; Salt Lake City. 2013. p. 127
38. Samsonov AA, Kholmovski EG, Parker DL, Johnson CR. POCSENSE: POCS-based reconstruction for sensitivity encoded MRI. Magn Reson Med. 2004; 52:1397–1406. [PubMed: 15562485]
39. Samsonov AA, Velikina J, Jung Y, Kholmovski EG, Johnson CR, Block WF. POCS-enhanced correction of motion artifacts in parallel MRI. Magn Reson Med. 2010; 63:1104–1110. [PubMed: 20373413]
40. Murphy M, Alley M, Demmel J, Keutzer K, Vasanawala S, Lustig M. Fast L_1-SPIRiT compressed sensing parallel imaging MRI: scalable parallel implementation and clinically feasible runtime. IEEE Trans Med Imaging. 2012; 31:1250–1262. [PubMed: 22345529]
41. Vasanawala SS, Alley MT, Hargreaves BA, Barth RA, Pauly JM, Lustig M. Improved pediatric MR imaging with compressed sensing. Radiology. 2010; 256:607–616. [PubMed: 20529991]
42. Zhang T, Pauly JM, Vasanawala SS, Lustig M. Coil compression for accelerated imaging with Cartesian sampling. Magn Reson Med. 2013; 69:571–582. [PubMed: 22488589]
43. Tofts PS. Modeling tracer kinetics in dynamics Gd-DTPA MR imaging. J Magn Reson Imaging. 1997; 7:91–101. [PubMed: 9039598]

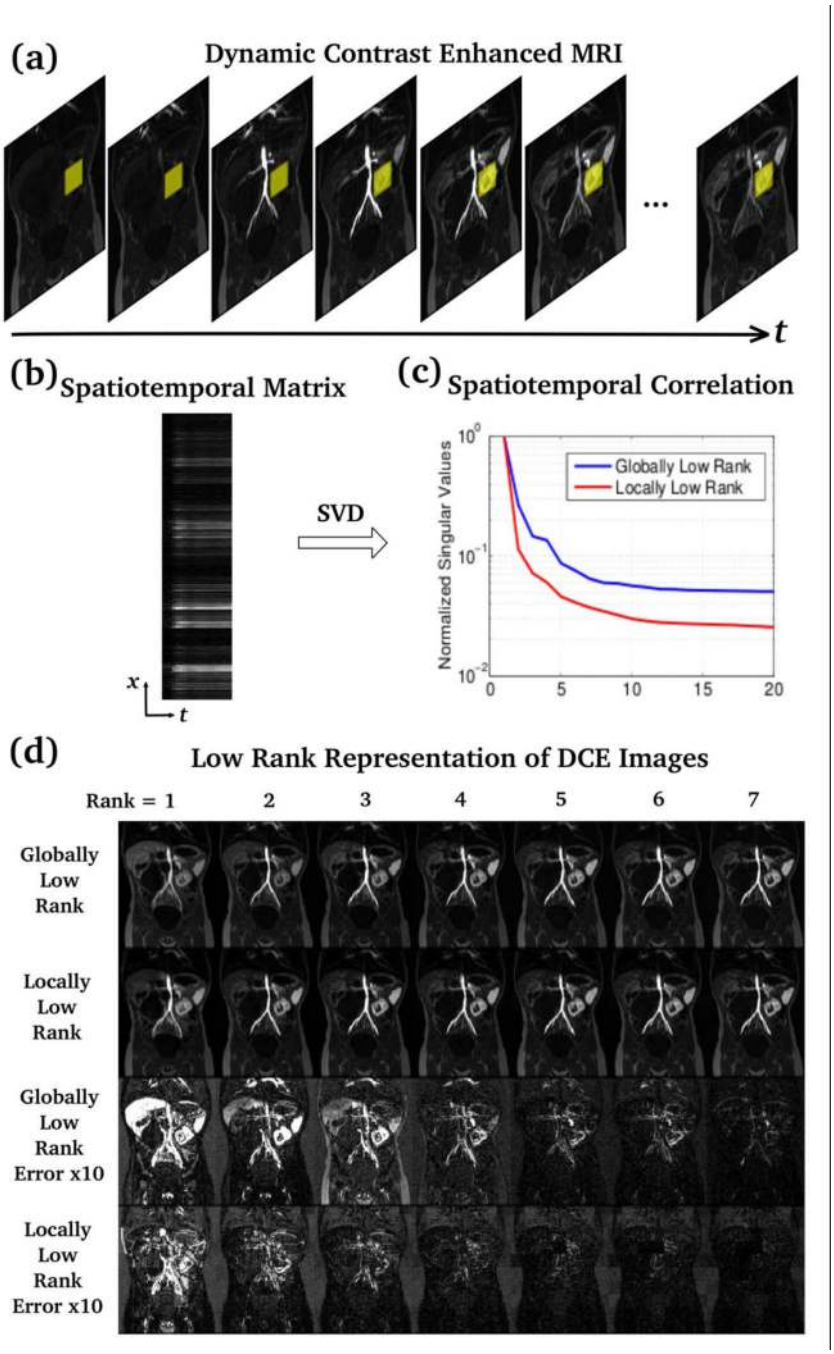

Figure 1.

Demonstration of the locally low rank property of DCE image series: (a) A series of 20 DCE images are acquired at different time points; (b) A selected image region (yellow block in (a)) is reformatted into a spatiotemporal matrix; (c) The singular values of the spatiotemporal matrices decrease dramatically after SVD. The spatiotemporal matrix from selected image region (red curve) in (b) has lower rank than that from the entire image (blue curve); (d) The original image series can be represented by using only few dominant

singular vectors. Accepting a root-mean-square error of 0.006, only four singular vectors were needed for LLR to represent the original 20 images, less than GLR.

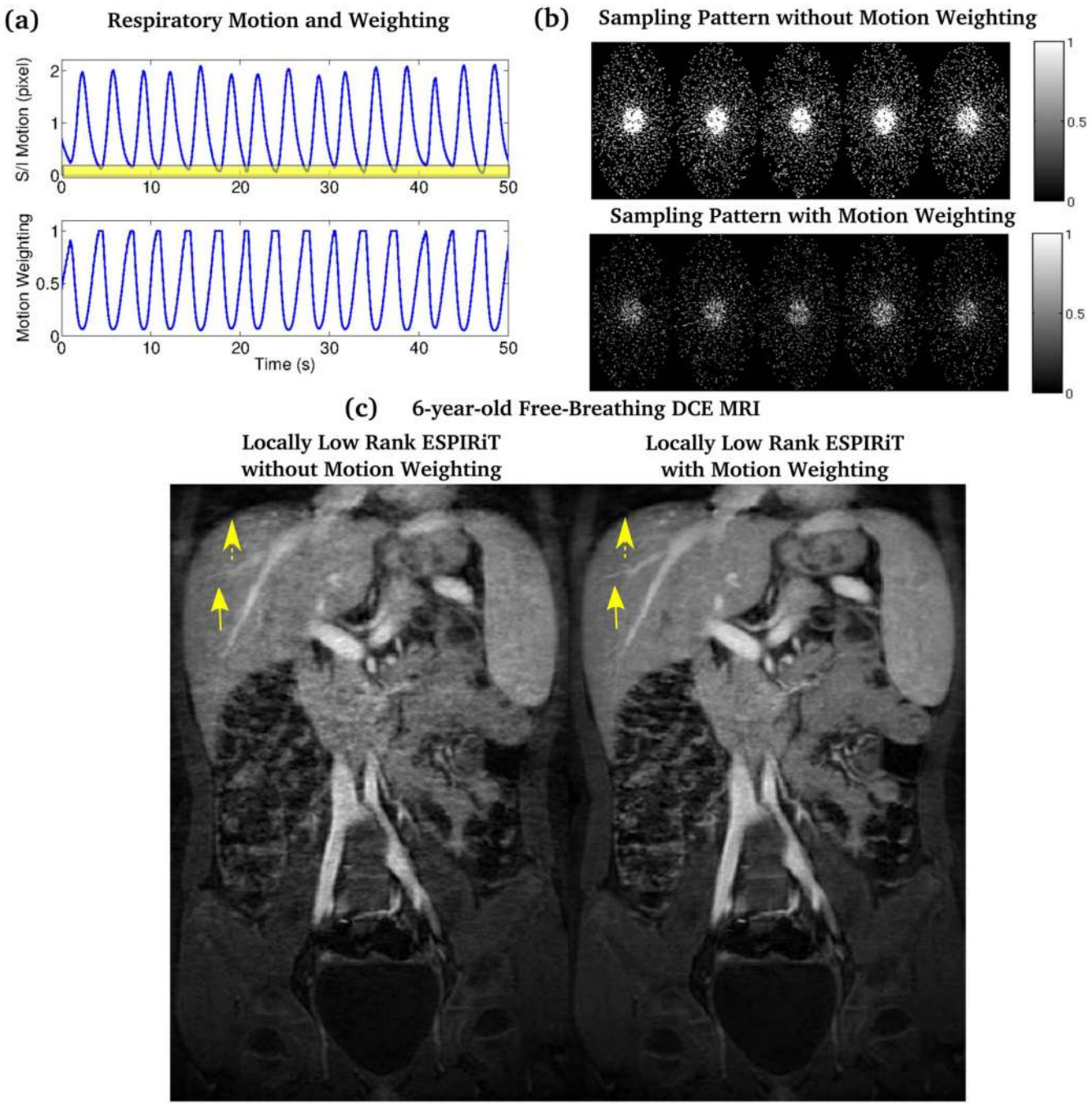

Figure 2.

Demonstration of the soft respiratory gating for free-breathing DCE of a 6-year-old patient: (a) top: respiratory motion in superior/inferior direction estimated by the Butterfly navigator (motion-free region highlighted); bottom: the corresponding weighting function for estimated respiratory motion; (b) The VDRad sampling pattern for the first five temporal phases without (top) and with (bottom) soft respiratory gating; (c) Locally Low Rank ESPIRiT reconstruction of a free-breathing DCE dataset with no motion weighting (left) and soft respiratory gating (right). Note that soft-gated Locally Low Rank ESPIRiT is much

sharper, with better delineation of fine vessels (solid arrows) and the edge of the liver (dash arrows).

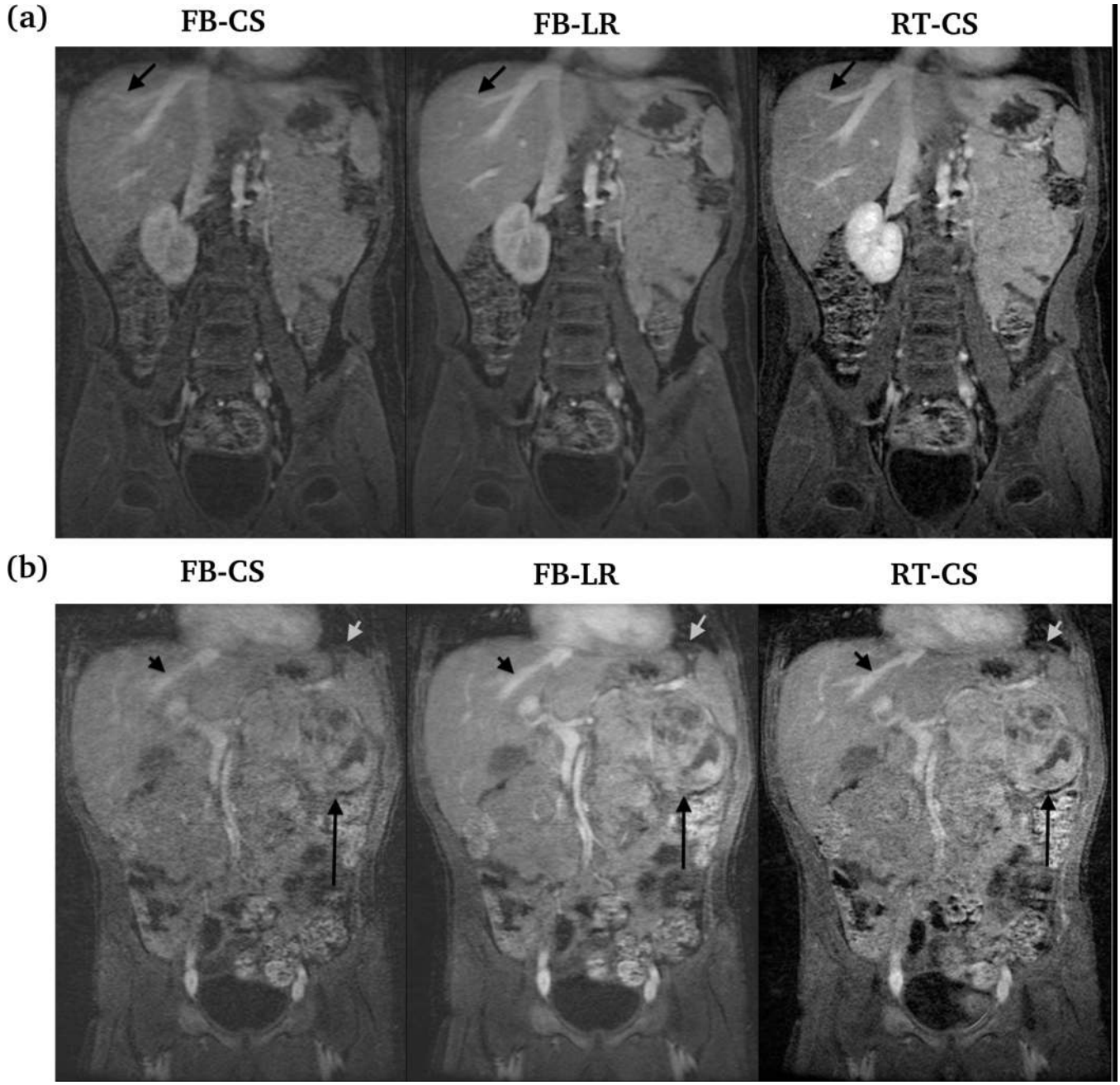

Figure 3.

Representative results of the free-breathing compressed sensing (FB-CS), free-breathing soft-gated low rank (FB-LR) and respiratory-triggered compressed sensing (RT-CS) reconstructions of (a) a 6-year-old male and (b) 5-year-old male. Good overall image quality of the free-breathing reconstructions was achieved. Because of the VDRad ordering, no obvious motion ghosts were noticed even in FB-CS without any motion correction. Note the improved delineation of annotated structures in FB-LR and RT-CS over FB-CS: (a) second order branches of the hepatic vein (black arrows); (b) left hemidiaphragm (light grey

arrows), first order branches of the hepatic vein (short black arrows), and a large left adrenal mass (long black arrows).

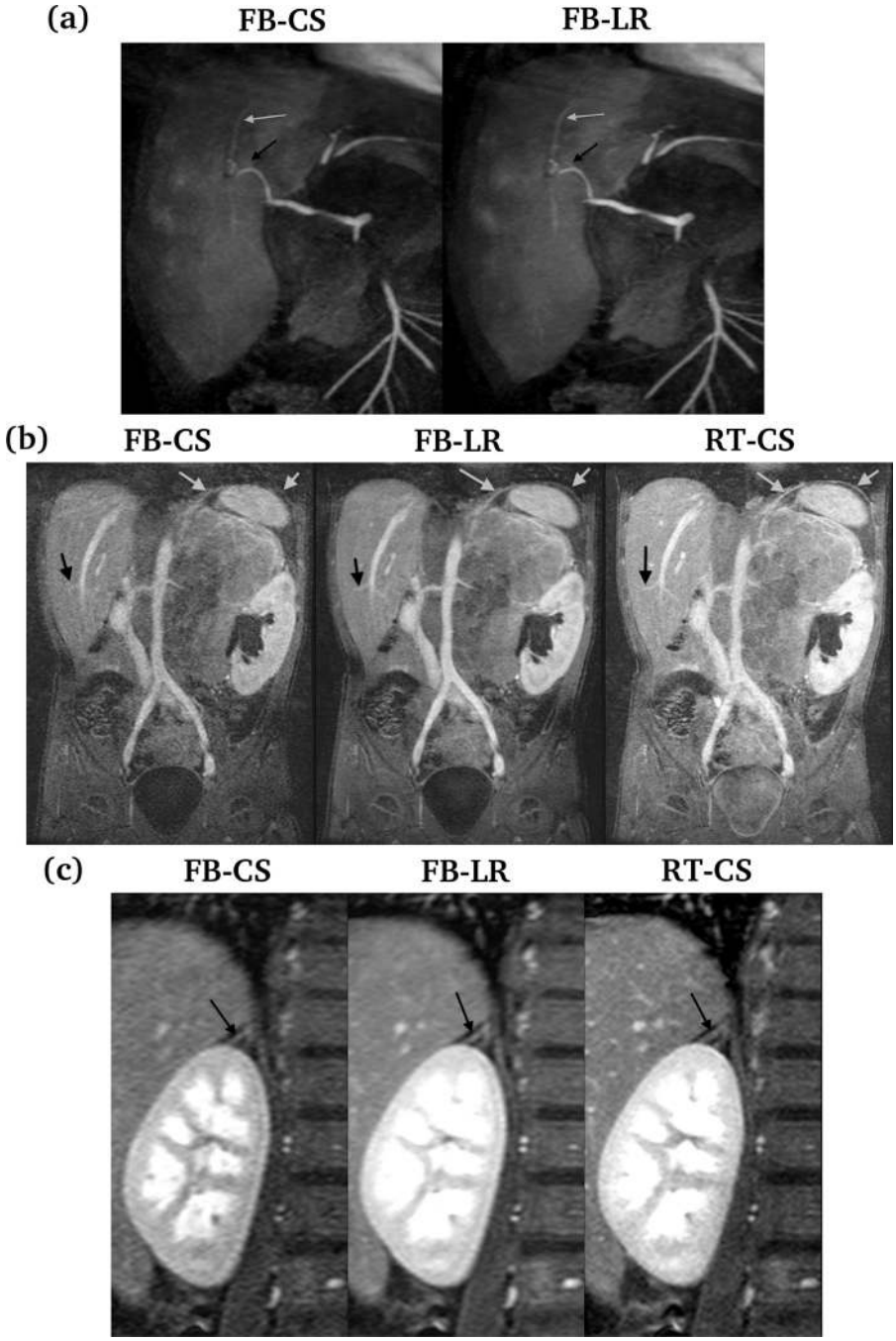

Figure 4.

Example of the comparisons of the structural delineations of FB-CS, FB-LR, and RT-CS. (a) A replaced right hepatic artery arising from the superior mesenteric artery is shown (arrows), better visualized by FB-LR (right). Arterial evaluation without venous contamination of the portal or hepatic veins was achieved because of the high temporal resolution of the proposed method. (b) Improved visualization of the left hemidiaphragm (light grey arrows) was achieved in FB-LR and RT-CS over FB-CS; peripheral branch of the hepatic vein (black arrows) was also better delineated in FB-LR and RT-CS than FB-CS. (c)

right adrenal gland (black arrows) was demonstrated the extent to which the individual limbs can be evaluated. Note that the lateral limb of the adrenal gland can be distinguished from adjacent structures in FB-LR and RT-CS.

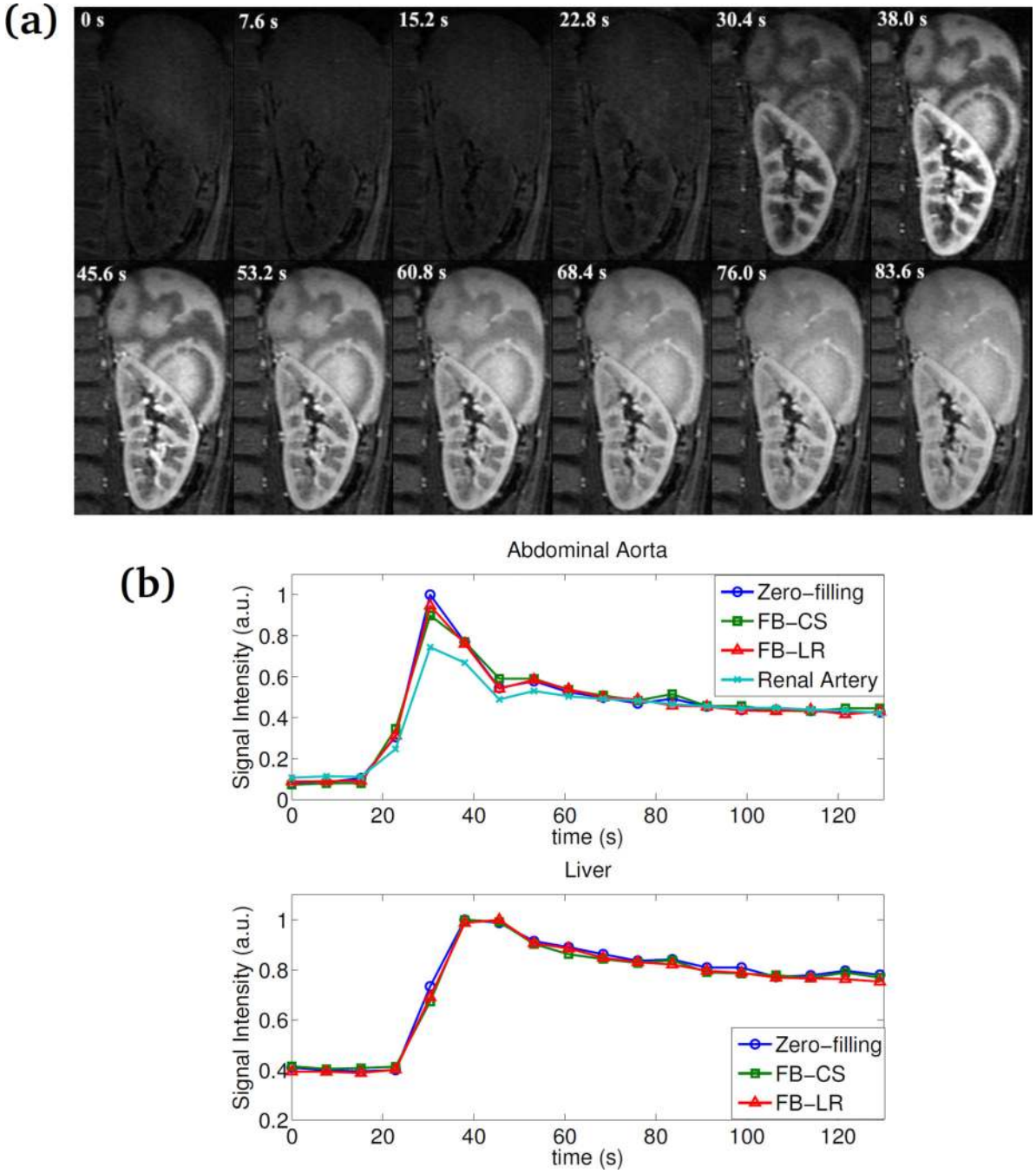

Figure 5.

Example of the FB-LR reconstruction of a 6-year-old patient. (a) A zoomed and cropped image of the spleen and kidney from the first 12 of 18 temporal phases are shown. The time of acquisition is shown on top of each image. The spatial resolution was 1.1×1.1 mm^2. The high temporal resolution is evidenced by the progressive enhancement from cortical to medullary region of the kidney, as well as the perfusion pattern of the spleen. (b) Contrast enhancement curves of the manually segmented abdominal aorta (top) and liver (bottom) from the zero-filling reconstruction, FB-CS and FB-LR are shown. The contrast dynamics of

FB-CS and FB-LR had good agreement with that of the zero-filling reconstruction. The contrast enhancement of the right renal artery in the FB-LR reconstruction (shown at the top) also matched that of the abdominal aorta.

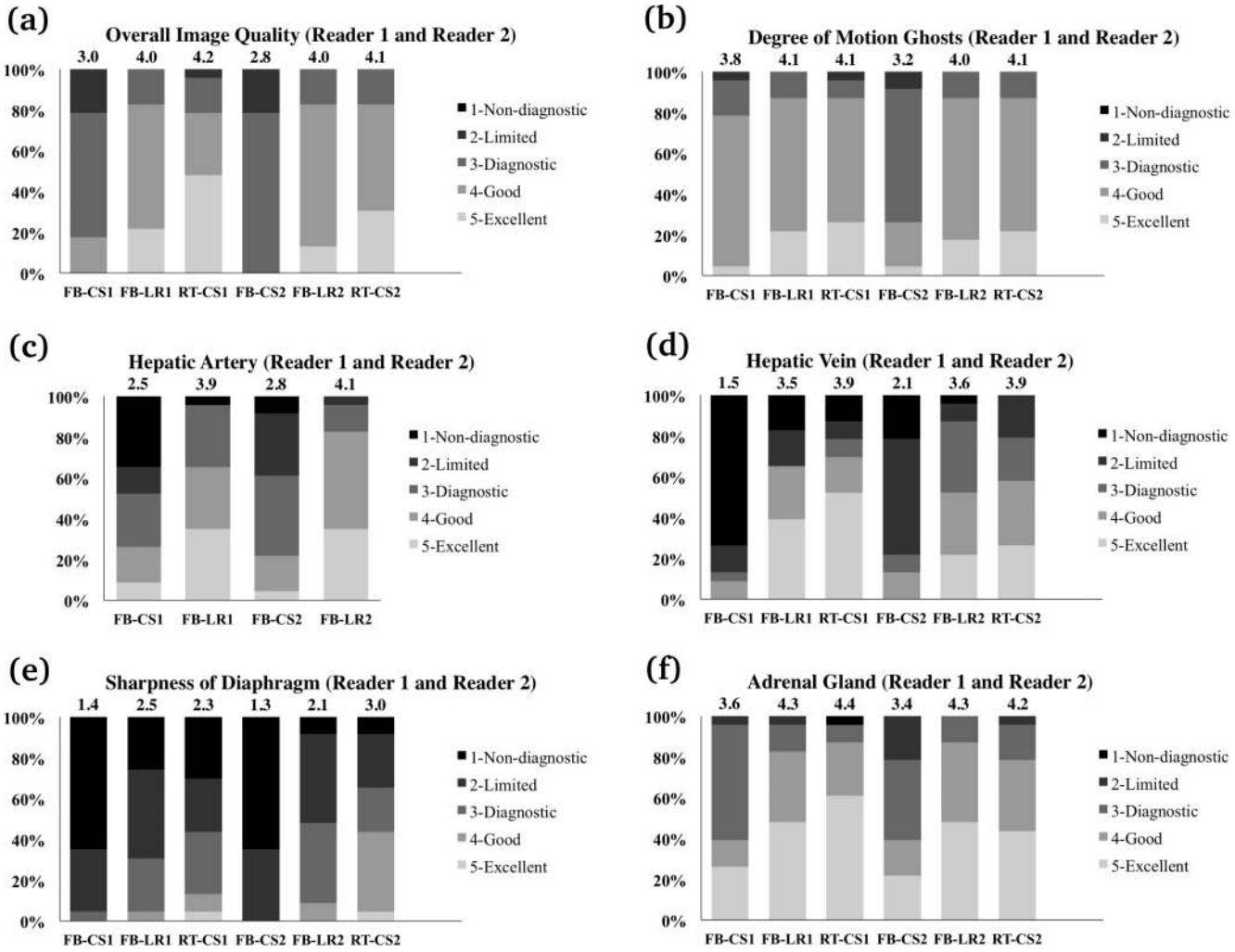

Figure 6.

Representative results of image assessments for FB-CS, FB-LR and RT-CS when evaluated independently from both readers: (a) overall image quality; (b) degree of non-cardiac motion ghosts; (c) hepatic artery; (d) hepatic vein; (e) sharpness of diaphragm; and (f) adrenal gland. Each color bar represents the percentage of the cases with the same score. The mean score of each reconstruction is shown on top of the color bar.

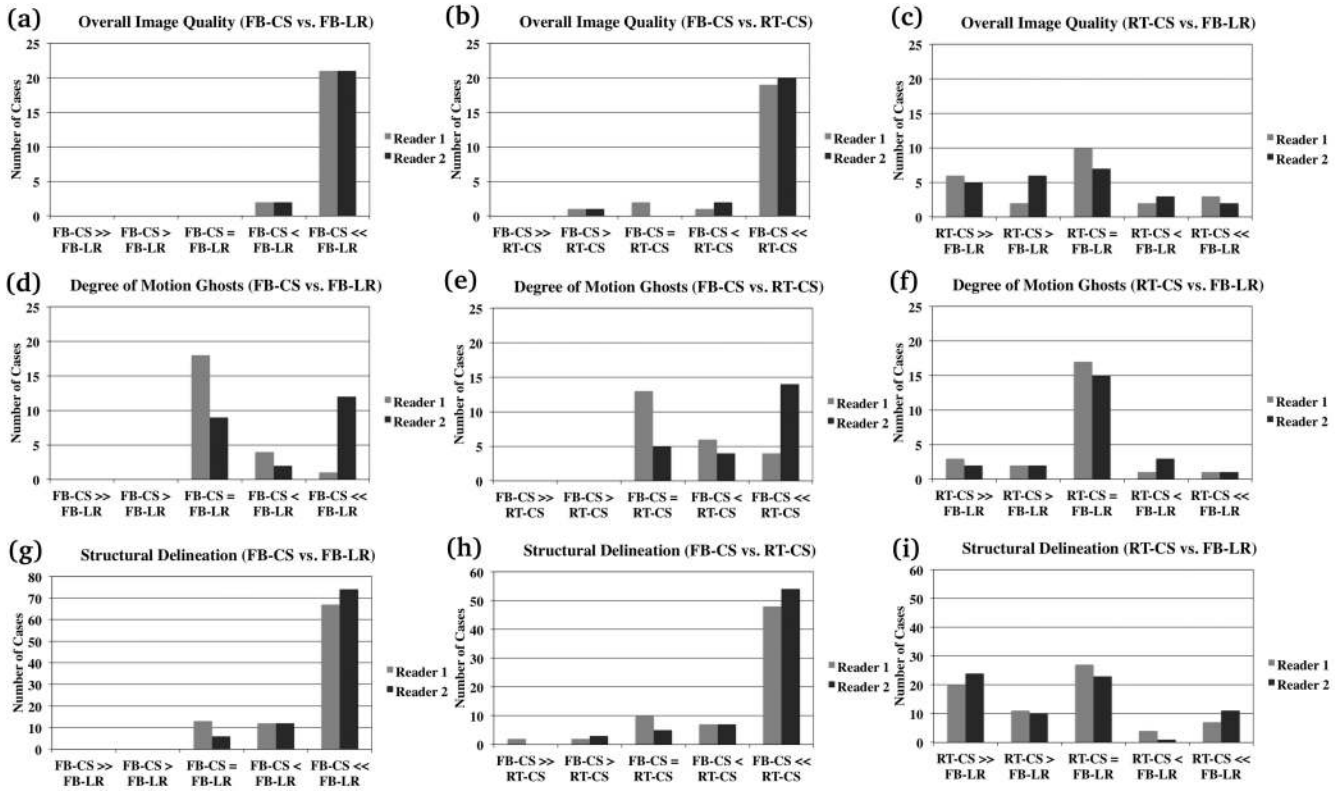

Figure 7.

Representative results of the paired assessments based on the scoring criteria in Tab. 3. Bar graphs were generated for the preference on overall image quality, degree of non-cardiac motion ghosts, and the combination of the delineation of four structures (hepatic artery, hepatic vein, diaphragm and adrenal gland). The scores of the preference (1, 2, 3, 4, 5) were represented by (≫, >, =, <, ≪) respectively in the bar graph. For example, "FB-CS ≫ FB-LR" means FB-CS was preferred and had better delineation than FB-LR. The preferences between FB-CS and FB-LR for both readers are shown in (a), (d) and (g). The preferences between FB-CS and RT-CS for both readers are shown in (b), (e) and (h). The preferences between RT-CS and FB-LR for both readers are shown in (c), (f) and (i).

Table 1

Demographics of patients, acquisition parameters, respiratory support and clinical indications

Subject Number	Age (years)	Gender	Slice Thickness (mm)	S/I FOV (cm)	Spatial Resolution (mm^2)	Frame Rate (s)	Respiratory Support*	Clinical Indication
1	6.5	M	0.9	36	1.1×1.1	7.6	LMA	Abdominal Mass
2	6.8	M	1.2	34	1.1×1.1	5.6	LMA	Neuroblastoma
3	2.8	M	1.2	28	0.9×0.9	5.4	NC	Neuroblastoma
4	5.0	M	1.2	29	0.9×0.9	7.4	NC	Neuroblastoma
5	0.1	F	1.2	20	0.6×0.6	5.4	ETT	Abdominal Mass
6	6.3	M	1.0	30	0.9×0.9	7.3	NC	Neuroblastoma
7	0.9	M	1.0	24	0.8×0.8	7.6	NC	Fever, right leg pain
8	8.6	F	1.2	44	1.4×1.4	7.3	LMA	Li-Fraumeni Syndrome
9	3.5	F	1.2	28	0.9×0.9	5.8	NC	Hepatoblastoma
10	2.5	M	1.2	32	1.0×1.0	5.9	ETT	Abdominal mass
11	5.3	M	1.2	32	1.0×1.0	6.9	LMA	AML Pre-transplant Workup
12	3.8	F	1.2	34	1.1×1.1	6.3	NC	Neuroblastoma
13	2.8	M	1.2	28	0.9×0.9	6.0	ETT	Cholangitis
14	1.9	F	1.2	28	0.9×0.9	5.6	LMA	Wilms
15	3.2	M	1.2	28	0.9×0.9	5.6	LMA	Hepatoblastoma
16	2.2	F	1.2	28	0.9×0.9	6.2	ETT	Hepatoblastoma
17	4.8	M	1.1	30	0.9×0.9	6.4	NC	Neuroblastoma
18	7.0	F	1.1	33	1.0×1.0	6.0	NC	Neuroblastoma
19	5.0	M	1.2	32	1.0×1.0	6.8	LMA	Clear Cell Sarcoma
20	4.8	M	1.2	28	0.9×0.9	7.1	ETT	Abdominal Mass
21	5.4	F	1.0	32	1.0×1.0	6.6	NC	Embryonal Rhabdomyosarcoma
22	8.8	F	1.2	32	1.0×1.0	6.4	LMA	Teratoma
23	2.9	F	1.2	28	0.9×0.9	6.9	LMA	CNS Tumor

*NC: nasal cannula; LMA: laryngeal mask; ETT: endotracheal tube

Table 2

Scoring criteria for image assessment when evaluated independently

Score	Overall image quality	Degree of coherent non-cardiac motion ghosts	Hepatic Artery	Hepatic Vein	Sharpness of diaphragm	Adrenal gland*
1 (Non-diagnostic)	Non-diagnostic assessment of all structures	Coherent ghosts limiting assessment of most structures	Main hepatic artery blurred	Right hepatic vein (RHV) blurred	Diaphragm totally obscured	Adrenal not visualized
2 (Limited)	Limited assessment of several structures	Coherent ghosts limiting assessment of several structures	Right hepatic artery (RHA) blurred	First order branches of RHV blurred	Less than 1/3 of diaphragm seen	One limb of adrenal visualized but blurry
3 (Diagnostic)	All but 1–2 structures can be assessed	Coherent ghosts limiting assessment of 1–2 structures	First order branches of RHA blurred	Sharp first order branches of RHV	1/3 – 2/3 diaphragm seen	Both limbs visualized but blurry
4 (Good)	All structures can be assessed	Minimally detectable ghosts	Sharp first order branches of RHA	Sharp second order branches of RHV	Larger than 2/3 of diaphragm seen	One limb visualized sharply
5 (Excellent)	Sharp delineation of all structures with high SNR and no non-cardiac motion artifacts	No detectable ghosts	Sharp second order branches of RHA	Braches visualized to within 1 cm of periphery	Entire right hemidiaphragm sharply seen	Both limbs visualized sharply

*Right adrenal gland was evaluated if present, otherwise left adrenal gland was evaluated.

Table 3

Scoring criteria of preference for paired side-by-side assessments*

Score	Image preference (Left vs. Right)
1	Images on the left was preferred and had better delineation than the images on the right
2	Images on the left was preferred but did not have better delineation than the images on the right
3	Images on the left and right were equivalent
4	Images on the right was preferred but did not have better delineation than the images on the left
5	Images on the right was preferred and had better delineation than the images on the left

*One reconstruction was presented on the left side of the screen and the other on the right side in a randomized blinded fashion for comparisons. Preferences for all evaluations in Tab. 2 were scored except hepatic artery.

Table 4

Inter-observer agreement results using weighted kappa coefficients between reader 1 and reader 2 for all qualitative image assessments

	FB-CS	FB-LR	RT-CS	FB-CS vs. FB-LR	FB-CS vs. RT-CS	RT-CS vs. FB-LR
Overall image quality	Moderate	Substantial	Substantial	Moderate	Substantial	Almost perfect
Degree of non-cardiac motion ghosts	Moderate	Almost perfect	Almost perfect	Fair	Fair	Almost perfect
Hepatic artery	Almost perfect	Substantial	-	Poor	-	-
Hepatic vein	Substantial	Substantial	Almost perfect	Substantial	Substantial	Substantial
Sharpness of diaphragm	Substantial	Substantial	Substantial	Fair	Substantial	Substantial
Adrenal gland	Almost perfect	Almost perfect	Substantial	Substantial	Almost perfect	Almost perfect

Table 5

Results of the Quantitative Analysis of Contrast Dynamics

Subject Number	Number of phases between hepatic artery and hepatic vein (FB-CS)	Number of phases between hepatic artery and hepatic vein (FB-LR)	RMSE of FB-CS (Aorta)	RMSE of FB-LR (Aorta)	RMSE of FB-CS (Liver)	RMSE of FB-LR (Liver)	Cross correlation between aorta and renal artery in FB-LR
1	3	3	0.032	0.017	0.017	0.013	0.995
2	7	7	0.049	0.050	0.029	0.020	0.999
3	7	7	0.046	0.040	0.021	0.019	0.996
4	6	6	0.038	0.046	0.015	0.026	0.999
5	7	7	0.037	0.054	0.016	0.016	0.994
6	7	7	0.037	0.068	0.019	0.024	0.998
7	10	10	0.040	0.040	0.017	0.018	0.996
8	9	9	0.038	0.066	0.017	0.020	0.994
9	9	9	0.036	0.048	0.018	0.007	0.999
10	6	6	0.042	0.055	0.015	0.023	0.996
11	8	8	0.038	0.042	0.031	0.018	0.998
12	6	6	0.059	0.057	0.021	0.014	0.998
13	4	4	0.038	0.040	0.015	0.018	0.993
14	8	8	0.040	0.057	0.017	0.020	0.998
15	8	8	0.053	0.053	0.009	0.032	0.998
16	6	6	0.042	0.045	0.022	0.030	0.998
17	5	5	0.082	0.062	0.020	0.022	0.998
18	11	11	0.053	0.060	0.014	0.013	0.999
19	7	7	0.039	0.056	0.016	0.019	0.999
20	4	4	0.048	0.050	0.034	0.024	0.997
21	7	7	0.031	0.032	0.027	0.027	0.999
22	11	11	0.062	0.047	0.026	0.016	0.997
23	6	6	0.063	0.056	0.011	0.019	0.999